Phonon thermal transport in Bi_{2}Te_{3} from first principles

Olle Hellman and David A. Broido

Phys. Rev. B **90**, 134309 — Published 17 October 2014

DOI: 10.1103/PhysRevB.90.134309

Phonon thermal transport in Bi_2Te_3 from first principles

Olle Hellman[1] and David A. Broido[2]

[1] *Department of Physics, Chemistry and Biology (IFM), Linköping University, SE-581 83, Linköping, Sweden.*

[2] *Department of Physics, Boston College, Chestnut Hill, Massachusetts 02467, USA*

We present first principles calculations of the thermal and thermal transport properties of Bi_2Te_3 that combine an ab initio molecular dynamics (AIMD) approach to calculate interatomic force constants (IFCs) along with a full iterative solution of the Peierls-Boltzmann transport equation for phonons. The newly developed AIMD approach allows determination of harmonic and anharmonic interatomic forces at each temperature, which is particularly appropriate for highly anharmonic materials such as Bi_2Te_3. The calculated phonon dispersions, heat capacity, and thermal expansion coefficient are found to be in good agreement with measured data. .The lattice thermal conductivity, κ_l, calculated using the AIMD approach nicely matches measured values, showing better agreement than the κ_l obtained using temperature independent IFCs. A significant contribution to κ_l from optic phonon modes is found. Already at room temperature, the phonon lineshapes show a notable broadening and onset of satellite peaks reflecting the underlying strong anharmonicity.

PACS numbers: 31.15.E-,61.48.-c,71.20.Tx,78.30.Na

I. INTRODUCTION

With dramatic advances in materials fabrication technology and computational power during the past two decades, materials for thermoelectric cooling and power generation have attracted significant interest. Since being identified as a promising thermoelectric material decades ago,[1] Bi_2Te_3 remains one of the best thermoelectrics available today with a measured figure of merit, ZT, of around 1 for bulk alloys of Bi_2Te_3 and maximum 1.4 in nanostructured form.[2] Recently, fabrication of atomically thin crystals of Bi_2Te_3[3] have introduced a new potentially promising avenue to tailor the thermoelectric properties of this Van der Waals bonded layered structure.

The remarkably high ZT that occurs in Bi_2Te_3 and related compounds arises in part because of their intrinsically low lattice thermal conductivities, κ_l, and accurate theoretical descriptions of κ_l in this class of materials are of critical importance. For decades, theories of κ_l introduced simple models and approximations that typically required a host of fit parameters, which were adjusted to measured data. However, in recent years, powerful first principles approaches have been developed to calculate κ_l, which have provided a deeper understanding of the nature of thermal transport in non-metallic crystals and their alloys. While these approaches[4–13] are effective for many materials, they may not be ideal for Bi_2Te_3 and related compounds because of such materials unusually large anharmonicity. To address this, here we calculate the κ_l for Bi_2Te_3 using a recently developed ab initio description that includes explicitly the temperature dependence of the interatomic forces[14–16]

In section II, the first principles theoretical approach used to determine the thermal and thermal transport properties of Bi_2Te_3 is developed. Section III presents the calculated results for Bi_2Te_3 including phonon dispersions, heat capacity, thermal expansion coefficient, thermal conductivity and phonon lineshapes. Summary and conclusions are given in section IV.

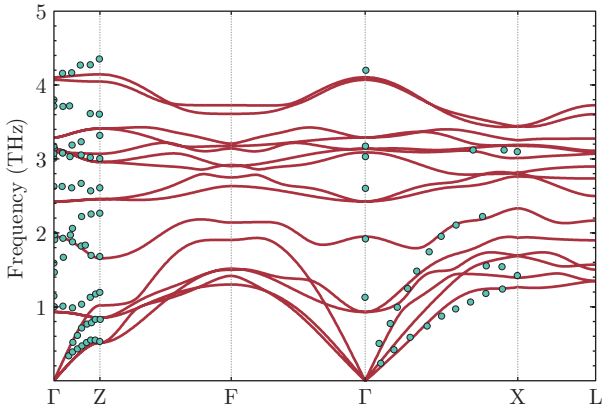

FIG. 1. Phonon dispersion relations along high symmetry directions for Bi_2Te_3 at calculated using AIMD determined IFCS at 77K (red curves) compared to measured data[17] also at 77K (green points).

II. THEORY

To obtain the thermal and thermal transport properties of Bi_2Te_3, accurate, temperature-dependent description of the harmonic and anharmonic interatomic forces combined with a full solution of the phonon Boltzmann transport equation (BTE) are used here, as detailed in the following two subsections.

A. Interatomic force constants

In previous ab initio calculations, the harmonic and anharmonic interatomic force constants (IFCs) have been

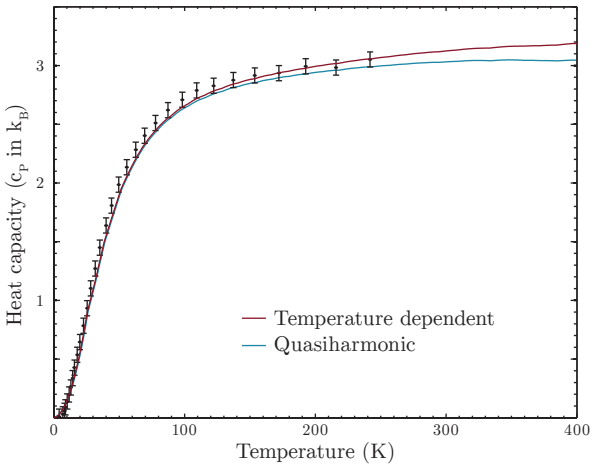

FIG. 2. Heat capacity, c_P, at constant pressure of Bi_2Te_3 as a function of temperature. Red curve gives the c_P obtained using IFCs obtained with the TDEP formalism; blue curve gives the c_P using IFCs determined within the QHA; points with error bars are measured data taken from Bessas *et al.* [18]

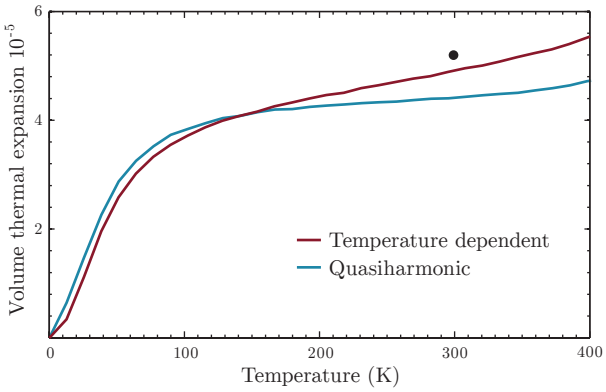

FIG. 3. The volume coefficient of thermal expansion for Bi_2Te_3 calculated using the AIMD approach (red curve) and with IFCs determined within the QHA (blue curve). The experimental point at 300K is from Bessas *et al.* [18]

obtained at the volume that minimizes the total electronic energy. Such an approach gives effectively T=0K IFCs. This approximation is reasonable as long as the material under study is not highly anharmonic, and it has been shown to work well for such materials. For highly anharmonic materials, the Born-Oppenheimer potential energy surface can show a considerable temperature dependence, which suggests that the lattice contributions should be included at each temperature considered. Here this is accomplished using a recently developed ab initio molecular dynamics approach.[14–16]

In this approach, a temperature-dependent anharmonic effective potential (TDEP) is constructed, and the IFCs in the model Hamiltonian are fit to the Born-Oppenheimer molecular dynamics potential energy surface at each temperature, making the technique suitable for calculations of important materials properties such as phonon lifetimes. The model Hamiltonian is chosen to be:

$$H = U_0 + \sum_i \frac{\mathbf{p}_i^2}{2m_i} + \frac{1}{2!}\sum_{ij\alpha\beta} \Phi_{ij}^{\alpha\beta} u_i^\alpha u_j^\beta + \frac{1}{3!}\sum_{ijk\alpha\beta\gamma} \Psi_{ijk}^{\alpha\beta\gamma} u_i^\alpha u_j^\beta u_k^\gamma \quad (1)$$

Here, m_i, p_i, and u_i are the mass, momentum and displacement from equilibrium of atom i, $\alpha\beta\gamma$ designate cartesian components, and Φ and Ψ are the second and third order effective IFCs. The explicit procedure for extracting these IFCs has been described previously in Refs. 14 and 16. We note that these IFCs will implicitly include renormalization to infinite order of anharmonicity, as well as all orders of electron-phonon coupling. This form of model Hamiltonian allows us to calculate the phonon dispersions, free energy, thermal expansion, phonon lifetimes and phonon thermal conductivity with an explicit temperature dependence.

All density functional theory calculations were done using the projector augmented wave (PAW)[19] method as implemented in VASP.[20–23] We treated exchange-correlation within the local density approximation (LDA)[24]. Bi_2Te_3 crystallizes in a layered hexagonal structure that can be reduced to a rhombohedral unit cell, defined with a lattice parameter a and an angle α, or equivalently a larger hexagonal unit cell defined by two lattice parameters, a and c. For the molecular dynamics it is beneficial to have a simulation cell as compact as possible, so we built the supercell from $4\times4\times1$ repetitions of the hexagonal unit cell, 96 Bi atoms and 144 Te in total. Harmonic IFCs were calculated out to 11 coordination shells, while anharmonic IFCs were calculated out to fifth coordination shells. Constraints due to translational invariance and other symmetries were employed to identify the minimum number of independent IFCs that needed to be computed, as described previously.[14,16] To properly treat the effect of temperature, we performed the calculations on a grid of 5 volumes, 4 angles and 4 temperatures. IFCs for temperatures and volumes between these grid points were obtained using interpolation.

Since Bi_2Te_3 is a layered material we tested a series of proposed van-der-Waals functionals, namely vdW-DF[25],optPBE-vdW[26],optB88-vdW,optB86-vdW[26], and vdW-DF2[27]. These functionals consistently give a bulk modulus 20-40% lower than the LDA values, resulting in too low phonon frequencies and consequently that do not agree well with experiment. As a result, we have not used these functionals.

For each of these grid-points, we ran *ab inito* molecular dynamics in the canonical ensemble. Temperature was controlled using a Nosé thermostat[29], and each point was run for about 10000 time steps of 2fs each. For the BZ integration we use the Γ-point and the plane-wave energy cutoff was set at 300eV. From each of these sets,

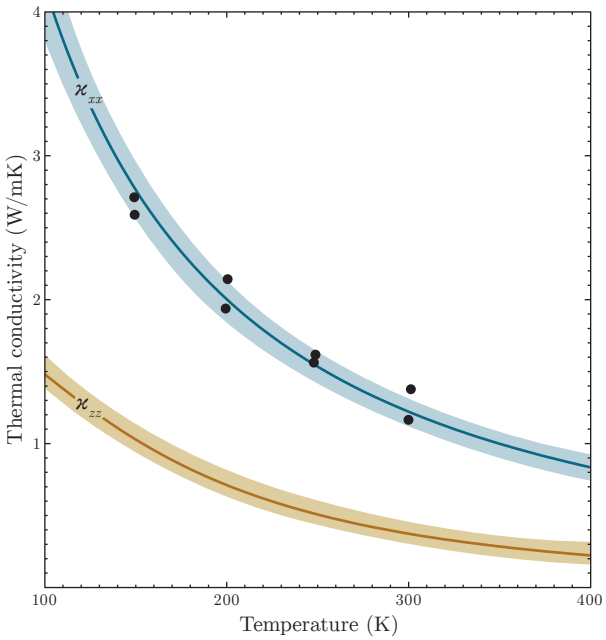

FIG. 4. The thermal conductivity calculated at zero pressure using T-dependent IFCs. The top line is the in-plane (κ_{xx}) and the bottom line the out-of-plane (κ_{zz}) thermal conductivity. In-plane experimental values from two samples (black circles) are from Goldsmid [28].

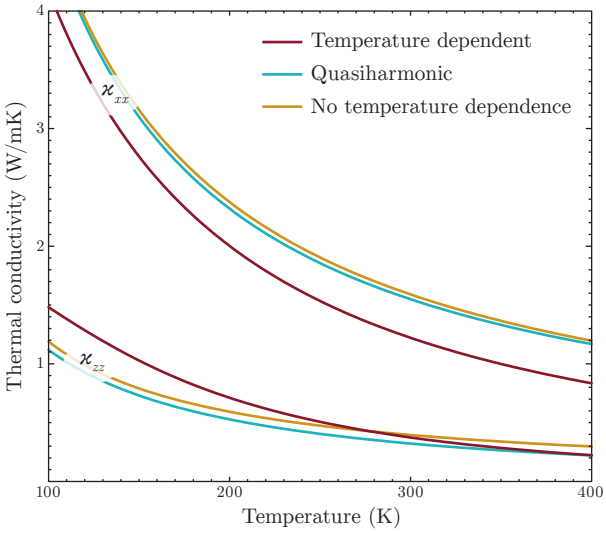

FIG. 5. Comparison of κ_{xx} (upper curves) and κ_{zz} (lower curves) using the temperature-dependent approach (red curves), the quasiharmonic approximation (blue curves) and temperature independent results (gold curves).

50 uncorrelated samples were chosen and recalculated using a $3 \times 3 \times 3$ k-point grid to achieve the desired accuracy.Using the TDEP method, we obtained the Gibbs free energy surface, $G(P,T)$, and in the process obtained volume and rhombohedral angle as a function of temperature. We translated this to a volume coefficient of thermal expansion, $\alpha = (1/V)\partial V/\partial T$. With the free energy surface, the harmonic and anharmonic IFCs are obtained at the equilibrium (P=0) pressure at each temperature. This allows immediate calculation of the phonon frequencies, heat capacity, $c_P = -T\partial^2 G/\partial T^2$, and volume Grüneisen parameters $\gamma_\lambda = -V/\omega_\lambda \partial\omega_\lambda/\partial V$, where λ designates the phonon mode with wave vector $\mathbf{q}$ and branch index s at each temperature.

B. Phonon lifetimes and thermal conductivity

We have examined phonon thermal transport in Bi_2Te_3 using the IFCs determined from the AIMD approach. The hexagonal symmetry of the Bi_2Te_3crystal structure gives a diagonal thermal conductivity tensor with in-plane and out of plane components, κ_{xx} and κ_{zz}, respectively. A temperature gradient, ∇T, is taken to be applied along x or z directions. The resulting phonon current in direction α through the sample is:

$$J_\alpha = \frac{1}{V}\sum_{\mathbf{q}s} \hbar\omega_{\mathbf{q}s} v_{\mathbf{q}s\alpha} n_{\mathbf{q}s\alpha} \tag{2}$$

where V is the crystal volume, $v_{\mathbf{q}s\alpha}$ is the phonon velocity in mode $\mathbf{q}s$, and $n_{\mathbf{q}s\alpha}$ is the non-equilibrium distribution function. For small thermal gradients ∇T_α, the distribution functions can be linearized as

$$n_{\mathbf{q}s\alpha} \approx n^0_{\mathbf{q}s} - v_{\mathbf{q}s\alpha}\tau_{\mathbf{q}s\alpha}\frac{dn^0_{\mathbf{q}s}}{dT}\frac{dT}{d\alpha} \tag{3}$$

where n^0 is the equilibrium (Bose) distribution at temperature T, α corresponds to a Cartesian direction and $\tau_{\mathbf{q}s\alpha}$ the phonon lifetime for transport in that direction.

The phonon lifetimes of Bi_2Te_3 are determined from a full, iterative solution of the phonon Boltzmann equation (PBE).[30] The phonon modes and three-phonon scattering rates are calculated at each temperature, since at each temperature the force constants, volume and rhombohedral angle will be different. The PBE was solved on a $15 \times 15 \times 15$ q-point grid for each of the temperatures. The momentum conservation is exactly fulfilled on an odd grid. For the energy conservation we tested two computational schemes: 1) The adaptive broadening scheme of Yates *et al.*[31], and 2) a tetrahedron approach.[32–34] Convergence as a function q-grid density was tested for each approach. For approach 1, this involved adjusting the adaptive broadening parameter so as to achieve converged thermal conductivity with increasing grid density. Both approaches converged to the same thermal conductivity values to within 1%. It was determined that the tetrahedron approach was computationally more efficient for systems with small numbers of atoms per unit cell, such as Si, whereas for materials with larger unit cells, such as Bi_2Te_3, the adaptive Gaussian scheme was preferable as it more easily handled the many branch crossings.

From the lifetimes, the lattice thermal conductivity is

calculated as:

$$\kappa_{\alpha\alpha} = \frac{1}{V}\sum_{\mathbf{q}s} C_{\mathbf{q}s} v^2_{\alpha\mathbf{q}s} \tau_{\alpha\mathbf{q}s} \quad (4)$$

where $C_{\mathbf{q}s} = \hbar\omega_{\mathbf{q}s}\partial n^0_{\mathbf{q}s}/\partial T$ is the mode specific heat.

III. RESULTS AND DISCUSSION

We have calculated the thermal and thermal transport properties of Bi_2Te_3 using IFCs determined using the AIMD approach. These results are compared with those obtained using 1) T=0K IFCs obtained at the volume that minimizes the the total electronic energy but not including thermal effects, and 2) using T-dependent IFCs obtained within the quasi-harmonic approximation (QHA) where the temperature dependence is incorporated indirectly through the volume dependence of the phonon frequencies. In all cases, anharmonic phonon-phonon scattering as well as scattering from isotopic impurities was included. The isotope scattering has negligible on effect κ_l is in this material even at the lowest temperatures considered.

Fig. 1 shows the Bi_2Te_3 phonon dispersions along high symmetry directions calculated using equilibrium harmonic IFCs determined using the AIMD approach for T=77K compared to experimental values measured also at 77K.[17] Relatively good agreement is seen throughout the Brillouin zone for both acoustic and optic phonon branches. The calculated transverse acoustic (TA) and longitudinal acoustic (LA) phonon velocities along $\Gamma \rightarrow X$ (in-plane) direction are 1.63 km/s and 2.65km/s and along $\Gamma \rightarrow Z$ (out of plane) are 1.37 km/s and 1.96 km/s. We note that the dispersions and acoustic velocities obtained here using AIMD compare well with previous results that did not include explicit T dependence in the IFCs.[35]

Fig. 2 gives the calculated heat capacity, c_P, of Bi_2Te_3 as a function of temperature compared to measured data.[18] It is evident that both AIMD and T=0K IFCs give excellent agreement with experiment over the full T range considered. This being said, above 100K, an increasing difference is seen between the C_P calculated using the two different approaches.

The calculated Bi_2Te_3 volume thermal expansion coefficient, α, is given as a function of T in Fig. 3 using IFCs determined using AIMD and within the QHA. It is evident that while both approaches give similar α for low T, above 200K, AIMD values are higher and have a larger slope than the QHA values reflecting the larger anharmonicity conveyed in the AIMD. In particular, at room temperature, they give better agreement with the measured α. Specifically, the calculated values at 300K for AIMD and QHA IFCs are $4.89 \cdot 10^{-5}\mathrm{K}^{-1}$ and $4.44 \cdot 10^{-5}\mathrm{K}^{-1}$, as compared to the measured value of $5.2 \cdot 10^{-5}$ K^{-1}.[18] Worth noting is that the measured values from various sources differ quite a bit, both in values and qualitative trends.[36]

Fig. 4 shows the in-plane and out-of-plane thermal conductivities, κ_{xx} and κ_{zz}, calculated with AIMD IFCs obtained at equilibrium for each temperature. The colored fields indicate the range of κ_{xx} and κ_{zz} when the lattice parameters are varied by $\pm 1\%$ from equilibrium.

It is evident that κ_{xx} and κ_{zz} are robust to such variations. Also shown are the κ_{xx} values measured by Goldsmid [28] for two Bi_2Te_3 samples. The AIMD calculated results show excellent agreement with these measured values over the full range of temperatures. The lower values of κ_{zz} compared to κ_{xx} arise in part because of the smaller out-of-plane acoustic velocities, as mentioned above and also due to the stronger anharmonicity in the out of plane direction, as reflected by the larger thermal expansion in this direction.

One might wonder if point defects in real Bi_2Te_3 samples could play a significant role in reducing its measured thermal conductivity. We have tested the sensitivity of the calculated lattice thermal conductivity of Bi_2Te_3 to such point defects. We find that it is quite insensitive to these, for both acoustic and optic phonons. Specifically, we have included up to 0.1% oxygen impurities as mass defects on both the Bi and Te sites. O atoms are about 8 (13) times lighter than Te (Bi) atoms. The large mass difference between O and Bi/Te and large defect concentration of 0.1% make this a particularly large perturbation,. Nevertheless, we find that the Bi2Te3 thermal conductivity decreases by a negligible amount (0.5% at 300K). The reason why the effect of point defects so small is that the anharmonic phonon-phonon scattering in Bi_2Te_3 around room temperature is extremely strong so the phonon-phonon scattering rates are much larger than the phonon-point defect scattering rates, even for relatively large concentrations of defects having large mass differences.

Recently, the lattice thermal conductivity of Bi_2Te_3 has been calculated using Green-Kubo molecular dynamics (MD) simulations with IFCs determined from empirical potentials developed from T=0K ab initio total energy surfaces.[4,5] In the 100K-400K temperature range, the calculated κ_{xx} values in Ref. 5 lie higher than the corresponding AIMD values obtained here while those from Ref. 4 are in reasonably good agreement with the AIMD values. The calculated κ_{zz} values in both Refs. 5 and 4 are larger than the corresponding AIMD values obtained here. In particular, at 300K, Ref. 5 gives κ_{xx}=2.4W/mK, while Ref. 4 gives κ_{xx}=1.3W/mK, almost identical to our κ_{xx} value obtained within the AIMD/BTE approach.

It is interesting to compare the lattice thermal conductivites obtained using AIMD IFCs at each temperature with the corresponding values obtained using T=0K IFCs calculated from total energy minimization and within the QHA. This is done in Fig. 5. In the 100K to 400K temperature range shown, κ_{xx} obtained from the T=0K IFCs (gold curve) is noticeably higher than that calculated using the AIMD IFCs (red curve).

This is due to subtle temperature dependent changes in the harmonic and anharmonic IFCs that arise in the

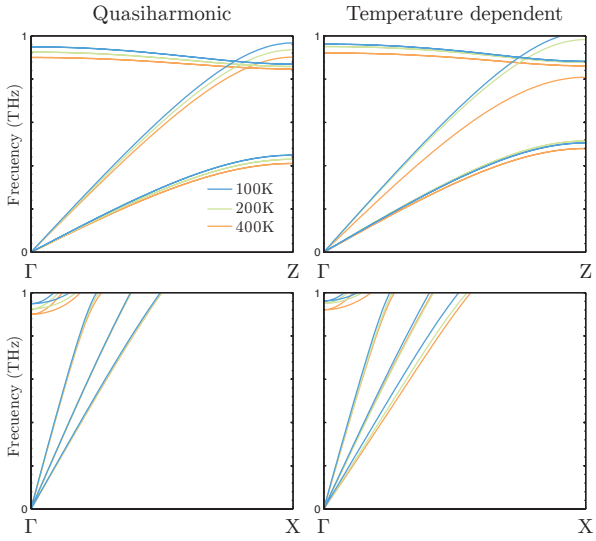

FIG. 6. The in plane and out of plane acoustic phonon dispersions vs temperature.

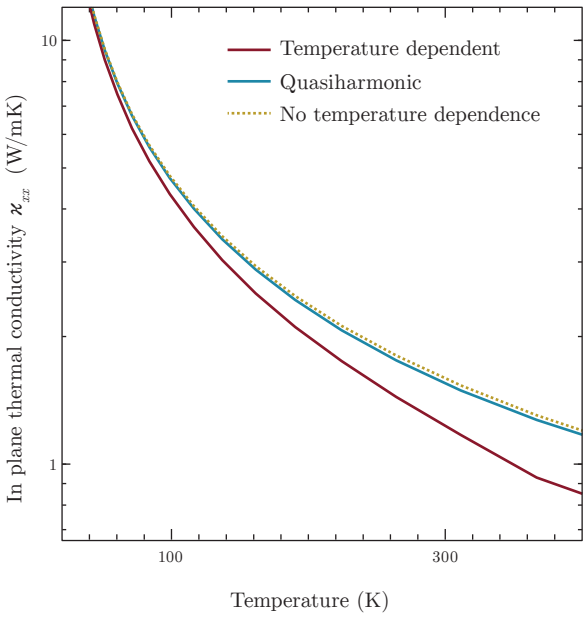

FIG. 7. κ_{xx} calculated using the temperature-dependent approach (red curve), and temperature-independent IFCs (gold curve) shown over an expanded temperature range to illustrate the increasing error introduced using the T-independent IFCs above about 100K.

AIMD calculations, which drive κ_{xx} to smaller values with increasing temperature. Specifically, the in-plane acoustic velocities become slightly smaller while the anharmonic IFCs become a slightly stronger. Understanding the interesting behavior of κ_{zz} is helped by examining the temperature dependence of the acoustic velocities, which are shown in Fig. 6 for the QHA and TDEP calculations. Along $\Gamma \rightarrow Z$, all of the acoustic branches obtained from the TDEP calculations are larger than those from the QHA at low temperature (100K). As a result, κ_{zz} is larger for the TDEP IFCs compared to that obtained using the QHA IFCs. However, with increasing temperature the LA velocities show substantial softening, which acts to lower κ_{zz} and produce the its more rapid decrease seen in Fig. 5.

The difference between the TDEP, QHA and T-independent results in Fig. 5 decreases with temperature as the effects of anharmonicity are reduced. This is illustrated in Fig. 7, which compares κ_{xx} values from the T=0K and QHA IFCs (gold and blue curves) with those from the T-dependent IFCs (red curve) over a large temperature interval. Below about 100K, the curves overlap. However, with increasing temperature, the TDEP curve show increasing separation from the other two, which highlights the importance of including the temperature dependence of the IFCs in the higher temperature range in order to accurately describe the thermal conductivity.

Recently developed experimental techniques can now measure the accumulation of the lattice thermal conductivity of a material as a function of the phonon mean free path (mfp).[37–39] Here we present the calculated accumulation for in-plane transport for Bi_2Te_3 calculated using the TDEP IFCs. The mfp of a phonon in mode $\mathbf{q}s$ is defined as $|\mathbf{v}_{\mathbf{q}s}|\tau_{\mathbf{q}s\alpha}$. The thermal conductivity accumulation, $\kappa^{\rm acc}(l)$, sums the fraction of heat carried by phonons with mfps smaller than l:

$$\kappa^{\rm acc}_{\alpha\alpha}(l) = \frac{1}{V}\sum_{\mathbf{q}s} C_{\mathbf{q}s} v^2_{\alpha\mathbf{q}s}\tau_{\alpha\mathbf{q}s}\Theta(l - |\mathbf{v}_{\mathbf{q}s}|\tau_{\alpha\mathbf{q}s}) \quad (5)$$

where $\Theta(x)$ is the Heaviside step function. Fig. 8 shows $\kappa^{\rm acc}_{xx}(l)$ at $T = 300K$. The separate curves show the per branch contributions, with yellow (green) shading giving the contributions for acoustic (optic) phonon branches. In many materials, direct contributions to κ_l from optic phonons are relatively small because optic phonon branches lie at higher frequencies so have lower thermal populations and are also less dispersive than acoustic phonon branches giving generally smaller optic phonon velocities.

In contrast, Fig. 8 shows that in Bi_2Te_3, large contributions to κ_{xx} are from optic phonons, a significant portion of which come from the lowest two optic branches. These findings are consistent with the relatively low frequencies of these two branches along with their being fairly dispersive compared to the other optic branches. Note that the two lowest lying optic branches are intertwined with the LA branch making it difficult to differentiate the contributions from acoustic and optic phonons in the frequency region between about 1-2 THz (see Fig. 1). We have indicated these contributions in purple in Fig. 8. The high-lying optic phonon branches (above around 2 THz), contribute about 20% of the total thermal conductivity at 300K. We estimate about an additional 10% contributionsfrom the two lowest optic branches giving a total of roughly 30%.

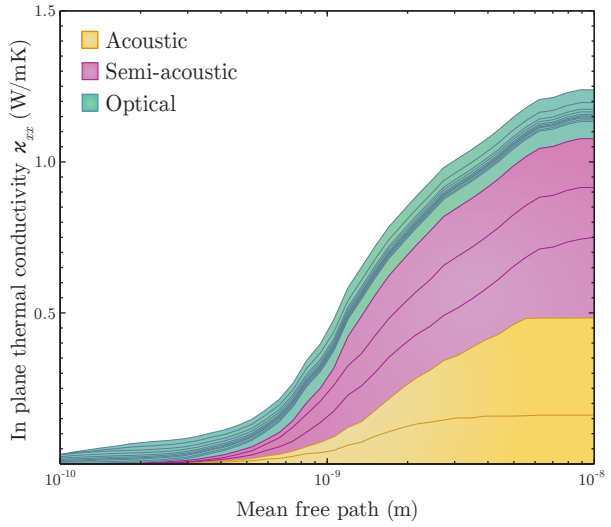

FIG. 8. Cumulative in-plane thermal conductivity κ_{xx} as a function of phonon mean free path at T=300K decomposed per phonon branch. Gold shaded region gives the contribution from the acoustic branches while the green shaded region gives the contribution from the optic branches. Purple shaded region gives mixed acoustic/optic phonon contributions, as described in the text.

It is interesting to note that 50% of the accumulation comes from phonons having mfps smaller than 1.5nm. This is in stark contrast to silicon where about 40% of the accumulation comes for phonons that are at least 1μm.[39] This large difference reflects the much smaller phonon lifetimes in Bi_2Te_3 compared to Si as well as the smaller Bi_2Te_3 acoustic velocities and frequencies.

The small mfp values contributing to κ_{xx} suggest that it would be hard to further reduce it through nanostructuring since the feature size would have to be smaller than the mfp of phonons contributing to the bulk intrinsinc κ_l. This is typically the case for low thermal conductivity bulk materials, as has been pointed out previously.[40]

Given the low frequency scale and strongly anharmonic nature of Bi_2Te_3 it is of interest to examine the phonon lineshapes. It is generally assumed that the phonon self energy $\Sigma = \Delta + i\Gamma$ will shift the frequencies ω by Δ and broaden the lines into Lorentzians with a FWHM of Γ. This is valid as long as $\Gamma \ll \omega$. To check the validity in Bi_2Te_3, we have calculated the phonon lineshapes, given by:[41]

$$\sigma_{\mathbf{q}s}(\Omega) \propto \frac{2\omega_{\mathbf{q}s}\Gamma_{\mathbf{q}s}(\Omega)}{\left(\Omega^2 - \omega_{\mathbf{q}s}^2 - 2\omega_{\mathbf{q}s}\Delta_{\mathbf{q}s}(\Omega)\right)^2 + 4\omega_{\mathbf{q}s}^2\Gamma_{\mathbf{q}s}^2(\Omega)} \tag{6}$$

where the imaginary part of the self-energy is given by

$$\begin{aligned}\Gamma_{\mathbf{q}s}(\Omega) = \sum_{s's''}\frac{\hbar\pi}{16}\frac{V}{(2\pi)^3}\iint_{\mathrm{BZ}}\left|\Psi_{ss's''}^{\mathbf{q}\mathbf{q}'\mathbf{q}''}\right|^2\Delta_{\mathbf{q}\mathbf{q}'\mathbf{q}''}\times \\ \Big[(n_{\mathbf{q}'s'}+n_{\mathbf{q}''s''}+1)\delta(\Omega-\omega_{\mathbf{q}'s'}-\omega_{\mathbf{q}''s''}) \\ +2(n_{\mathbf{q}'s'}-n_{\mathbf{q}''s''})\delta(\Omega-\omega_{\mathbf{q}'s'}+\omega_{\mathbf{q}''s''})\Big]d\mathbf{q}'d\mathbf{q}'',\end{aligned} \tag{7}$$

where $\Delta_{\mathbf{q}\mathbf{q}'\mathbf{q}''}$ ensures that $\mathbf{q}+\mathbf{q}'+\mathbf{q}''=K$, a reciprocal lattice vector, and the three-phonon matrix elements by

$$\begin{aligned}\Psi_{ss's''}^{\mathbf{q}\mathbf{q}'\mathbf{q}''} = \sum_{ijk}\sum_{\alpha\beta\gamma}\frac{\epsilon_{\alpha i}^{\mathbf{q}s}\epsilon_{\beta j}^{\mathbf{q}'s'}\epsilon_{\gamma k}^{\mathbf{q}''s''}}{\sqrt{m_i m_j m_j}\sqrt{\omega_{\mathbf{q}s}\omega_{\mathbf{q}'s'}\omega_{\mathbf{q}''s''}}}\times \\ \Psi_{ijk}^{\alpha\beta\gamma}e^{i\mathbf{q}\cdot\mathbf{r}_i+i\mathbf{q}'\cdot\mathbf{r}_j+i\mathbf{q}''\cdot\mathbf{r}_k}\end{aligned} \tag{8}$$

The real part of the self energy is given by a Kramers-Kronig transformation:

$$\Delta(\Omega) = \frac{1}{\pi}\int\frac{\Gamma(\omega)}{\omega-\Omega}d\omega \tag{9}$$

We calculated the lineshape (related to the inelastic neutron cross section) as a function of q along high symmetry directions in the Brillouin zone for temperatures of 77K, 300K and 450K. The results can be seen in Fig. 9.

At 77K the lineshapes are distinct and well-defined, but by 300K, there is notable broadening of the linewidths and some slight satellite peaks. At 450K the dispersions are significantly broadened to the point where most modes are completely diffuse. The anomalous anharmonicity at room temperature underlines the importance of including the temperature dependence of the IFCs. Some modes are diffuse beyond recognition, but the dispersive heat carrying modes still seem to have coherent behaviour and can be described with perturbation theory despite the strong anharmonicity.

IV. SUMMARY AND CONCLUSIONS

The thermal and thermal transport properties of Bi_2Te_3 have been calculated using a first principles approach that compares three different ways to determine of the harmonic and anharmonic interatomic force constants. Specifically, results obtained using IFCs from an AIMD approach are compared to those obtained using T=0K IFCs and those calculated within the quasi-harmonic approximation.

Using the AIMD calculated IFCs, good agreement with measured data is obtained for phonon dispersions, heat capacity, thermal expansion coefficient and lattice thermal conductivity and their deviation from those obtained with T-independent IFCs is particularly noticeable above room temperature. The latter two quantities show noticeably better agreement with experiment compared to corresponding results obtained using temperature independent IFCs. Their low frequency scale and relatively

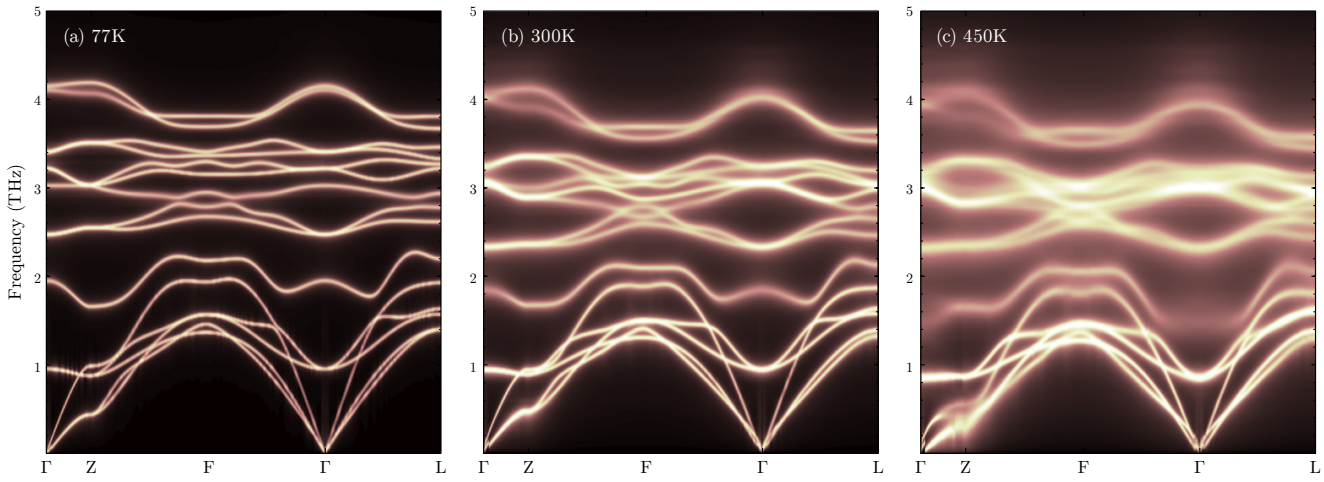

FIG. 9. Bi_2Te_3 phonon lineshapes at temperature 77, 300 and 450K in panels (a), (b) and (c) respectively. Brighter color reflects higher intensity.

dispersive behavior causes the optic phonon branches to provide a large contribution to the thermal conductivity of Bi_2Te_3 at room temperature. At and above room temperature, the phonon lineshapes show a notable broadening and satellite peaks highlighting the underlying strong anharmonicity.

V. ACKNOWLEDGMENTS

O.H. acknowledges support from the Knut & Alice Wallenberg Foundation (KAW) project "Isotopic Control for Ultimate Material Properties" and the Swedish Foundation for Strategic Research (SSF) program SRL10-002 is gratefully acknowledged. Supercomputer resources were provided by the Swedish National Infrastructure for Computing (SNIC). D.A.B. acknowledges support from the S3TEC, an Energy Frontier Research Center funded by the US Department of Energy, Office of Science, Office of Basic Energy Sciences under Award No. DE-FG02-09ER46577.

[1] H. J. Goldsmid and R. W. Douglas, British Journal of Applied Physics **5**, 386 (1954).
[2] B. Poudel, Q. Hao, Y. Ma, Y. Lan, A. J. Minnich, B. Yu, X. Yan, D. Wang, A. Muto, D. Vashaee, X. Chen, J. Liu, M. S. Dresselhaus, G. Chen, and Z. Ren, Science (New York, N.Y.) **320**, 634 (2008).
[3] D. Teweldebrhan, V. Goyal, M. Rahman, and A. A. Balandin, Applied Physics Letters **96**, 053107 (2010).
[4] B. Qiu and X. Ruan, Physical Review B **80**, 165203 (2009).
[5] B.-L. Huang and M. Kaviany, Physical Review B **77**, 125209 (2008).
[6] D. A. Broido, M. Malorny, G. Birner, N. Mingo, and D. A. Stewart, Applied Physics Letters **91**, 231922 (2007).
[7] A. Ward, D. A. Broido, D. A. Stewart, and G. Deinzer, Physical Review B **80**, 1 (2009).
[8] W. Li, N. Mingo, L. Lindsay, D. A. Broido, D. A. Stewart, and N. A. Katcho, Physical Review B **85**, 195436 (2012).
[9] T. Luo, J. Garg, J. Shiomi, K. Esfarjani, and G. Chen, EPL (Europhysics Letters) **101**, 16001 (2013).
[10] X. Tang and J. Dong, Proceedings of the National Academy of Sciences of the United States of America **107**, 4539 (2010).
[11] J. Shiomi, K. Esfarjani, and G. Chen, Physical Review B **84**, 104302 (2011).
[12] L. Lindsay, D. A. Broido, and T. Reinecke, Physical Review Letters **109**, 1 (2012).
[13] W. Li, L. Lindsay, D. A. Broido, D. A. Stewart, and N. Mingo, Physical Review B **86**, 174307 (2012).
[14] O. Hellman, P. Steneteg, I. A. Abrikosov, and S. I. Simak, Physical Review B **88**, 144301 (2013).
[15] O. Hellman, I. A. Abrikosov, and S. I. Simak, Physical Review B **84**, 180301 (2011).
[16] O. Hellman, P. Steneteg, I. A. Abrikosov, and S. I. Simak, Physical Review B **87**, 104111 (2013).
[17] W. Kullmann, G. Eichhorn, H. Rauh, R. Geick, G. Eckold, and U. Steigenberger, physica status solidi (b) **162**, 125 (1990).
[18] D. Bessas, I. Sergueev, H.-C. Wille, J. Perß on, D. Ebling, and R. P. Hermann, Physical Review B **86**, 224301 (2012).
[19] P. E. Blöchl, Physical Review B **50**, 17953 (1994).
[20] G. Kresse, Computational Materials Science **6**, 15 (1996).
[21] G. Kresse, Physical Review B **59**, 1758 (1999).
[22] G. Kresse and J. Furthmüller, Physical Review B **54**, 11169 (1996).

[23] G. Kresse and J. Hafner, Physical Review B **48**, 13115 (1993).
[24] D. M. Ceperley and B. Alder, Physical Review Letters **45**, 566 (1980).
[25] J. Klimeš, D. R. Bowler, and A. Michaelides, Physical Review B **83**, 195131 (2011).
[26] J. Klimeš, D. R. Bowler, and A. Michaelides, Journal of physics. Condensed matter : an Institute of Physics journal **22**, 022201 (2010).
[27] K. Lee, E. D. Murray, L. Kong, B. I. Lundqvist, and D. C. Langreth, Physical Review B **82**, 081101 (2010).
[28] H. J. Goldsmid, Proceedings of the Physical Society. Section B **69**, 203 (1956).
[29] S. Nosé, Molecular Physics **52**, 255 (1984).
[30] M. Omini and A. Sparavigna, Physica B: Condensed Matter **212**, 101 (1995).
[31] J. Yates, X. Wang, D. Vanderbilt, and I. Souza, Physical Review B **75**, 195121 (2007).
[32] P. E. Blöchl, Physical Review B **49**, 16223 (1994).
[33] P. Lambin and J. Vigneron, Physical Review B **29**, 3430 (1984).
[34] S. Lee, K. Esfarjani, J. Mendoza, M. S. Dresselhaus, and G. Chen, Physical Review B **89**, 085206 (2014).
[35] X. Chen, D. Parker, and D. J. Singh, Physical Review B **87**, 045317 (2013).
[36] L. M. Pavlova, Y. I. Shtern, and R. E. Mironov, High Temperature **49**, 369 (2011).
[37] A. J. Minnich, J. A. Johnson, A. J. Schmidt, K. Esfarjani, M. S. Dresselhaus, K. A. Nelson, and G. Chen, Physical Review Letters **107**, 095901 (2011).
[38] J. A. Johnson, A. A. Maznev, J. Cuffe, J. K. Eliason, A. J. Minnich, T. Kehoe, C. M. S. Torres, G. Chen, and K. A. Nelson, Physical Review Letters **110**, 025901 (2013).
[39] K. T. Regner, D. P. Sellan, Z. Su, C. H. Amon, A. J. H. McGaughey, and J. A. Malen, Nature communications **4**, 1640 (2013).
[40] Z. Tian, J. Garg, K. Esfarjani, T. Shiga, J. Shiomi, and G. Chen, Physical Review B **85**, 184303 (2012).
[41] R. A. Cowley, Reports on Progress in Physics **31**, 123 (1968).